Preprint Cambridge Centre for Computational Chemical Engineering ISSN 1473 – 4273

Detailed characterisation of TiO_2 nano-aggregate morphology using TEM image analysis

Manoel Y. Manuputty [1,4], Casper S. Lindberg [1,4], Maria L. Botero [3,4], Jethro Akroyd [1,4], Markus Kraft [1,2,4]

released: 30 October 2018

[1] Department of Chemical Engineering
and Biotechnology
University of Cambridge
West Site, Philippa Fawcett Drive
Cambridge, CB3 0AS
United Kingdom
E-mail: mk306@cam.ac.uk

[2] School of Chemical and
Biomedical Engineering
Nanyang Technological University
62 Nanyang Drive
637459
Singapore

[3] Department of Mechanical Engineering
National University of Singapore
9 Engineering Drive 1
117575
Singapore

[4] Cambridge Centre for Advanced Research
and Education in Singapore (CARES)
CREATE Tower, 1 Create Way
138602
Singapore

Preprint No. 213

UNIVERSITY OF CAMBRIDGE

Keywords: TiO_2, premixed flame, TEM, image analysis, nano-aggregates

Edited by
Computational Modelling Group
Department of Chemical Engineering and Biotechnology
University of Cambridge
West Site, Philippa Fawcett Drive
Cambridge, CB3 0AS
United Kingdom

Fax: + 44 (0)1223 334796
E-Mail: c4e@cam.ac.uk
World Wide Web: http://como.cheng.cam.ac.uk/

Abstract

A detailed morphological characterisation is performed on TiO_2 nano-aggregates synthesised in a premixed stagnation flame using transmission electron microscopy (TEM) image analysis. The size-dependent collection efficiency of the TEM sampling method is accounted for with a simple correction for particle deposition through impaction and diffusion. The TEM-derived sizes show excellent agreement with electrical mobility measurements. Primary particle size, aggregate size, and degree of aggregation distributions were obtained for two different flames and varying precursor loading. The degree of aggregation is defined as the ratio of gyration to spherical equivalent sizes from the projected area analysis, allowing identification of particles with spherical and non-spherical morphologies. The size distributions are found to be strongly affected by precursor loading but not by flame mixture or maximum temperature. In all cases, approximately 60–70% particles have spherical morphology while the rest form small aggregates. Aggregation is likely to occur only very late in the growth stage, leading to the similarity between the primary particle and spherical particle size distributions. The detailed morphological information reported provides the much-needed experimental data for studying the early stage particle formation of TiO_2 from titanium tetraisopropoxide (TTIP) in a well-defined burner configuration.

Highlights

- A TEM sampling method is presented which relies on impaction and diffusion mechanisms for particle deposition.
- A semi-automated image analysis algorithm is employed for aggregate morphological characterisation.
- The ratio of gyration to spherical equivalent sizes from projected area analysis is proposed as a measure of particle sphericity/degree of aggregation.
- Detailed morphological information generated includes primary particle size, aggregate size, and degree of aggregation distributions.

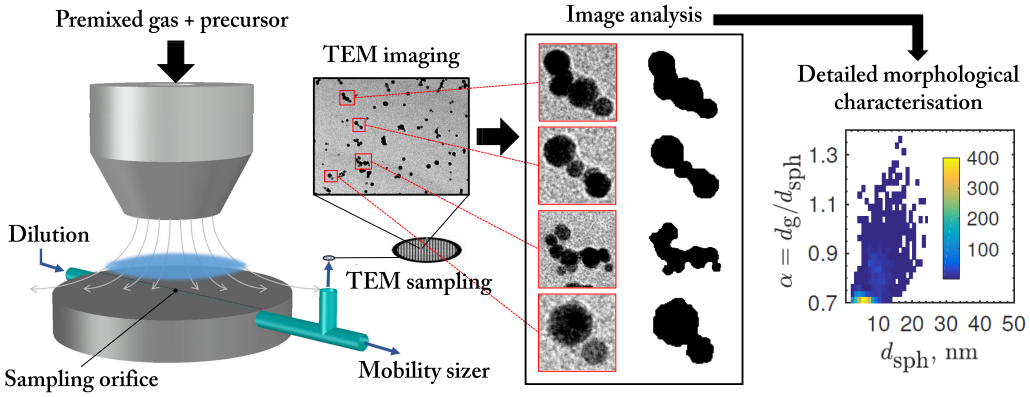

Contents

1 Introduction

Combustion synthesis has received significant focus in the research community as a way to prepare functional metal oxide nanoparticles such as titanium dioxide (TiO_2) [16, 35]. In order to design and exploit this process, understanding of the complex chemical and physical processes involved in the conversion of gaseous precursor molecules to solid particulates is required. One common strategy is to develop comprehensive models of the combustion system, including a description of particle population dynamics, guided by experimental observations [14, 40].

Particle population dynamics is modelled by a set of equations containing the description of the particles, also known as population balance equations [14]. In modelling a real system, where experimental data is available, some simplifications of particle representation are typically required to make the problem solvable [26]. The simplest representation is the spherical model where a particle is described only by its mass (given the density is known). This allows the number of equations to be reduced and solved with moment-based methods [9, 22]. This description can be extended in different ways to account for non-spherical morphology, for example with surface-volume models [37, 38, 41]. However, these simplifications often require making assumptions which are not always correct, such as particle monodispersity or power-law relationships for fractal-like aggregates, leading to additional uncertainties in the evaluation of the model predictions.

Alternatively, particles can be represented as an aggregate consisting of connected primary particles which can be solved stochastically [4, 26, 27, 34]. This detailed description resembles the actual structure of particles in experiments and thus the morphological properties can be derived without making any assumptions. Recently, Lindberg et al. [20] proposed a new detailed particle model where the coordinates of individual primary particles are tracked and thus the full particle morphology can be resolved. This method has been demonstrated for modelling the particle population dynamics for premixed stagnation flame experiments [11, 19, 42]. However, the level of details that the model is capable of resolving requires comparison against similarly detailed morphological measurements which are currently lacking in the literature.

Experimentally, premixed stagnation flames have been used to prepare TiO_2 nanoparticles from titanium tetraisopropoxide (TTIP) with particle sizes of 4–15 nm [13, 23, 25, 36]. The small particle size and narrow distribution are a result of a very short particle residence time, ideal for studying the early stages of particle formation. In addition, the pseudo one-dimensional flow enables the coupling between the particle model with the detailed gas-phase chemistry and flow dynamics at relative ease. Our previous modelling study demonstrated that the particle size is highly sensitive to the rate of surface reaction [22]. Thus, such flame with a well-defined and controllable configuration is suitable for comparison with model predictions to improve our understanding of TiO_2 formation in the combustion synthesis.

Various methods have been used to study TiO_2 formation in a premixed stagnation flame, including electrical mobility sizer [36, 44], mass spectrometry [13], laser diagnostics [31], electron microscopy [25, 43], and X-ray diffraction [23, 25, 43]. Among these, electron microscopy imaging (i.e. TEM) is most suitable to investigate the particle morphology

[29, 39] as it reveals the actual structure of particles, albeit as 2D projection. For example, TEM image analysis has been widely used in the combustion community to measure morphological properties of soot, such as aggregate size and fractal dimension [2, 6, 8, 12]. The main challenges with TEM measurements are the sensitivity to the sampling technique [29] and the difficulty in achieving statistically significant sample size. The former can be addressed by comparison against other diagnostic methods while the latter can be improved by using automated image analysis algorithms [5, 39].

The purpose of this paper is to develop an experimental methodology for a detailed characterisation of TiO_2 nanoparticle morphology prepared in a stagnation flame reactor which is lacking in the literature. Here we perform measurements of primary particle size, aggregate size, and degree of aggregation distributions using TEM measurements and image analysis. Such measurements provide important insights into particle growth processes and provide the much-needed morphological information for model evaluation.

The rest of this paper is structured as follows. Section 2 describes the experimental setup and the sampling procedures. Section 3 outlines the TEM image analysis algorithms used. Section 4.1 discusses the validation of the TEM sampling methodology by comparison with the electrical mobility measurements and Section 4.2 presents the morphological descriptions of the particles. Finally, the conclusions of this work are given.

2 Experimental methods

Figure 1 shows a schematic of the premixed laminar stagnation flame used in this study. Briefly, an aerodynamic nozzle (1.4 cm exit diameter) generated a laminar jet of premixed mixture that impinged on a water-cooled stagnation plate. Upon ignition, a thin flame was formed and stabilised by stretch above the stagnation plate. The setup used here is similar to that used in previous studies of titania and soot formation [7, 25, 36].

Two different flames were employed in this study with equivalence ratios of $\phi = 0.35$ (3.5% C_2H_4–30% O_2–66.5% Ar) and $\phi = 1.67$ (10.3% C_2H_4–18.5% O_2–71.2% Ar), corresponding to fuel-lean and fuel-rich conditions, respectively. The two different flames were used to investigate the effect of flame temperature with the rich flame being approximately 450 K hotter than the lean flame based on the calculated adiabatic flame temperature ($T_{ad} = 2073$ K and 2542 K [23]). The total gas flowrate was 28 slpm with a N_2 sheath flowrate of 20 slpm. The burner-surface separation, H, was 1 cm. The surface temperature, measured with a K-type thermocouple, was stabilised at 503±20 K ($\phi = 0.35$) and 580±20 K ($\phi = 1.67$). The flame standing distance was approximately 3.2±0.2 mm ($\phi = 0.35$) and 4.0±0.2 mm ($\phi = 1.67$). For each flame, titanium tetraisopropoxide (TTIP, Sigma Aldrich, 97%) was injected into the gas line with a syringe pump (Cole-Parmer) at three loading rates (4, 12, 30 ml/h, corresponding to 194, 582, and 1455 ppm of TTIP). The gas line was heated to 150°C to prevent precursor condensation. Previous studies have shown that the particles synthesised in the lean flame are mainly anatase while particles prepared in the rich flame are mainly mixtures of rutile and the metastable phase TiO_2-II [23].

Post-flame gas was sampled through a 0.2 mm orifice on a horizontal sampling probe

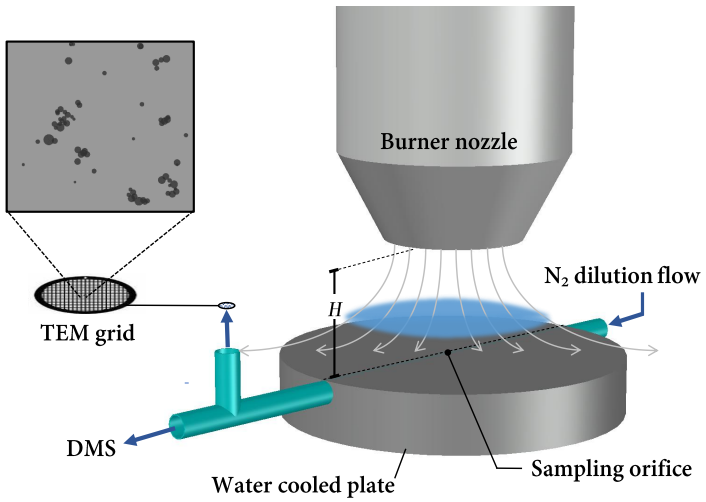

Figure 1: *A schematic of the premixed laminar stagnation flame synthesis and particle sampling method used in this study. The burner-stagnation surface separation distance, H, is 1 cm.*

inside the stagnation plate as shown in Fig. 1. The pressure drop across the orifice was maintained at 3 mbar under atmospheric pressure. A nitrogen flow of 35 slpm was used to quench the sampled gas to minimise further reactions after sampling and particle losses due to coagulation and wall deposition. Dilution tests were performed to determine the nitrogen flow rate for the operating conditions used. Downstream from the sampling orifice, a needle valve and vacuum pump system was configured to allow 8 slpm of the diluted flow to pass to a DMS500 (Cambustion Ltd.) for electrical mobility size measurements. Simultaneously, the remaining diluted gas was passed through a TEM grid (HC400-Cu, Electron Microscopy Sciences) mounted perpendicular to the flow within the sample line where particles were deposited and subsequently imaged for analysis. The holey carbon grids were chosen to allow sufficient particle collection for analysis. The sampling time for each measurement was 10–15 s. TEM micrographs were obtained with a JEOL JEM-2100F operating at 200 keV.

3 Image analysis

The image analysis procedures for primary particle size distribution and aggregate size distributions were performed on different sets of TEM images. For primary particle size analysis, approximately 20–30 images with 150,000× magnification were used (0.13 nm/pixel resolution) with minimum particle count of approximately 1100. The images were taken near the edge of holes on the carbon membrane to ensure sufficient contrast and particle concentration.

For aggregate size analysis, magnifications of 80,000× (0.24 nm/pixel), 60,000× (0.32 nm/pixel), and 40,000× (0.47 nm/pixel) were used for 4, 12, and 30 ml/h TTIP loading cases, respectively. The different magnifications were chosen to maintain a similar pixel count

per particle across the TTIP loadings tested. Approximately 100 images per sample were used with minimum particle count of approximately 1500 (see Table 4). The images for aggregate analysis were taken on the area of the membranes without holes while ensuring a maximum coverage of 5% to minimise particle overlap.

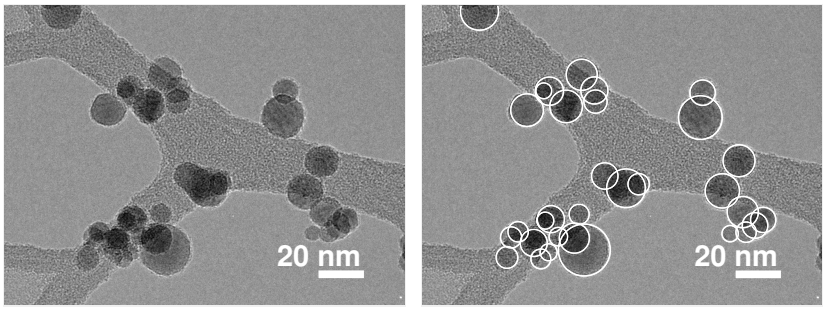

(a) A TEM image with 150,000× magnification.

(b) An annotated image showing spherical primary particles.

Figure 2: *TEM images showing primary particle size measurement procedure employed ($\phi = 1.67$, 30 ml/h TTIP loading rate).*

Primary particle size analysis For primary particle size analysis, the measurement of primary particle diameter, d_p, was performed using a MATLAB user interface by specifying the center of the sphere and a point on the circumference manually. The uncertainty of the measured d_p from manual measurement is estimated to be ± 2 pixel or ± 0.25 nm. Figure 2 shows an example of TEM images with spherical primary particles annotated. Due to the limited resolution of the TEM imaging, only particles larger than 3 nm were clearly distinguishable and measured. The average diameter ($\overline{d}_p$), Sauter mean diameter ($\overline{d}_{32}$), standard deviation (SD), and geometric standard deviation (GSD) were calculated for each case as follows,

$$\overline{d}_p = \frac{1}{N}\sum_{i=1}^{N} d_{p,i} \tag{1}$$

$$\overline{d}_{32} = \frac{\sum_{i=1}^{N} d_{p,i}^3}{\sum_{i=1}^{N} d_{p,i}^2} \tag{2}$$

$$\mathrm{SD} = \sqrt{\frac{1}{N-1}\sum_{i=1}^{N} |d_{p,i} - \overline{d_p}|^2} \tag{3}$$

$$\mathrm{GSD} = \exp\sqrt{\frac{1}{N}\sum_{i=1}^{N}\left(\ln\frac{d_{p,i}}{\mu_g}\right)^2}, \tag{4}$$

where $d_{p,i}$ is the spherical equivalent diameter of an individual primary particle, N is the total number of primary particles measured, and μ_g is the geometric mean of the measured data set $\{d_{p,1}, d_{p,2}, ..., d_{p,N}\}$.

Aggregate size analysis For aggregate projected area analysis, the following semi-automated procedures were employed (see Fig. 3 for illustration) using built-in functions in MATLAB Image Processing Toolbox [24],

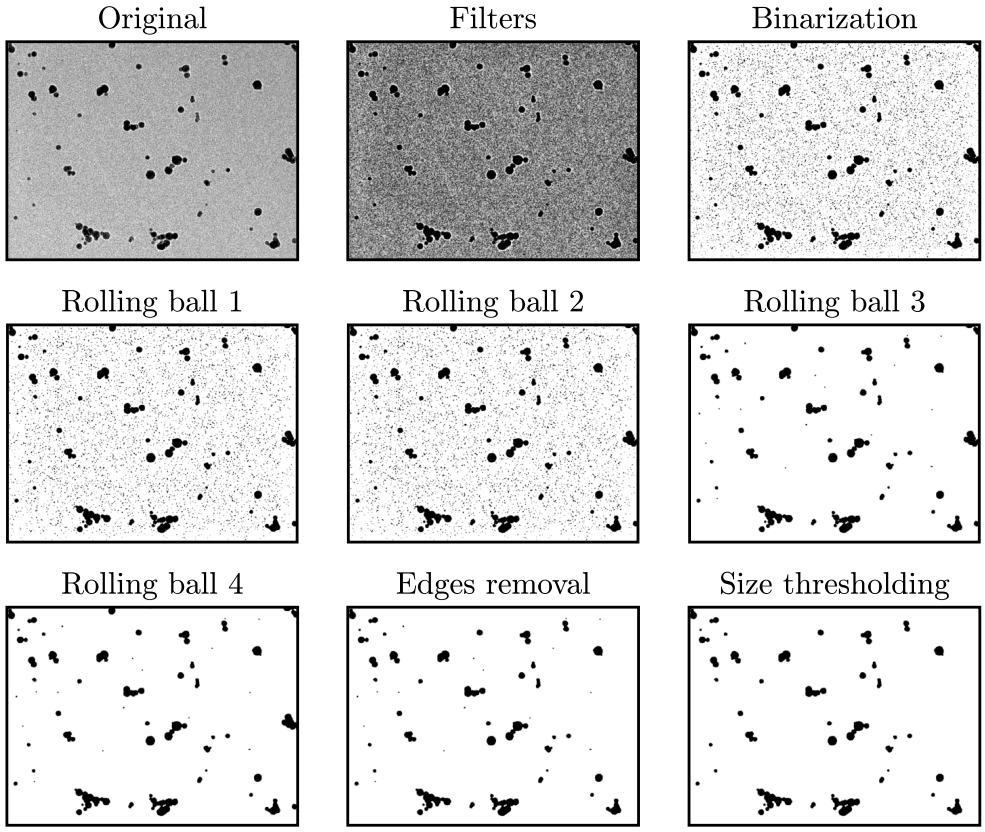

Figure 3: *Snapshots of an analysed TEM image ($\phi = 1.67$, 30 ml/h TTIP loading rate) at different stages of the projected area analysis procedure.*

1. **Filters**: Perform a contrast-limited adaptive histogram equalization (*adapthisteq* function) on 3×3 pixel tiles followed by a 2-D median filtering (*medfilt2* function) on 4×4 pixel tiles to enhance image contrast and reduce "salt and pepper" noise.

2. **Binarization**: Create a binary image with adaptive image threshold calculated using local first-order image statistics around each pixel (*imbinarize* function). A dark foreground polarity and a sensitivity parameter of 0.05 were specified.

3. **Rolling ball 1-4**: Restructure connected black pixels with four successive rolling ball transformations (*strel* function, [10]) with increasing disk size of 0.6 (rolling ball 1), 0.8 (rolling ball 2), 1.2 (rolling ball 3), and 1.6 nm (rolling ball 4).

4. **Edges removal**: Remove pixel blobs that touch the image edges to exclude aggregates that are not completely within the image frame.

5. **Size thresholding**: Remove structures with spherical equivalent diameter smaller than a specified threshold (2, 3, and 4 nm for 4, 12, and 30 ml/h loading rates, respectively).

6. Lastly, in the rare instance that the algorithm results in structures that are not particles (e.g., from clustered noise), these false particles are removed manually.

From the aggregate analysis, a data set $\{\mathbf{P}_1, \mathbf{P}_2, ..., \mathbf{P}_N\}$ was obtained where $\mathbf{P}_i$ contains a list of coordinates of the constituent pixels of aggregate i: $\{(x_{i,1}, y_{i,1}), (x_{i,2}, y_{i,2}), ..., (x_{i,L}, y_{i,L})\}$. The projected spherical equivalent diameter ($d_{\text{sph},i}$) and the projected diameter of gyration ($d_{g,i}$) of aggregate i were calculated as follows,

$$d_{\text{sph},i} = 2s\sqrt{\frac{L}{\pi}} \tag{5}$$

$$d_{g,i} = s\sqrt{\frac{1}{L}\sum_{j=1}^{L}\left(|x_{i,j} - \overline{x_i}|^2 + |y_{i,j} - \overline{y_i}|^2\right)} \tag{6}$$

$$(\overline{x_i}, \overline{y_i}) = \frac{1}{L}\sum_{j=1}^{L}(x_{i,j}, y_{i,j}), \tag{7}$$

where s is the image scale factor (nm per pixel) and L is the total number of pixels for aggregate i. Additionally, a parameter α_i was defined as the ratio of $d_{g,i}$ to $d_{\text{sph},i}$, which is indicative of the degree of aggregation of an analysed particle. A perfect circle has a characteristic $\alpha = \sqrt{1/2} \approx 0.707$. However, calculation of radius of gyration according to Eq. 6 tends to be an overestimate for a pixelated circle with less than 100 pixels and thus the value of α is expected to be slightly larger than 0.707 (this is discussed further in Section 4.2). The average aggregate projected area, $\overline{d}_{\text{sph}}$, and the average projected aggregate gyration diameter, $\overline{d}_g$, were calculated as follows,

$$\overline{d}_{\text{sph}} = \frac{1}{N}\sum_{i=1}^{N} d_{\text{sph},i} \tag{8}$$

$$\overline{d}_g = \frac{1}{N}\sum_{i=1}^{N} d_{g,i}, \tag{9}$$

where N is the total number of aggregates identified in the analysis.

4 Results and discussion

4.1 Validation of TEM sampling methodology

The TEM sampling methodology employed in this work is distinct to thermophoretic sampling commonly used for in-situ particle sampling [2, 3, 6]. Instead of thermophoresis, the particle deposition here relies on two main physical mechanisms, namely inertial impaction and Brownian diffusion as the sample flow through the holey TEM grid suspended perpendicular to the flow direction. It is assumed that interception can be ignored here given the size of the holes on TEM grid is typically much larger than the particles [32].

Due to the size dependency of inertial impaction and Brownian diffusion, it is necessary to perform a correction to the particle size distributions obtained using this methodology. However, as demonstrated below, the narrow size distribution produced with the stagnation flame configuration combined with the high sampling flow velocity results in a minimal correction. In this section, the overall collection efficiency of the holey TEM is estimated using similar approach used by Ogura et al. [28]. Subsequently, the corrected particle size is validated by comparison with the electrical mobility diameter measured with the DMS.

4.1.1 Correction for TEM collection efficiency

Taking into account Brownian diffusion and inertial impaction, assuming both mechanisms act independently, the overall collection efficiency, E, can be expressed as

$$E = 1 - (1 - E_{\mathrm{D}})(1 - E_{\mathrm{I}}), \tag{10}$$

where E_{D} is the collection efficiency due to Brownian diffusion, and E_{I} is the collection efficiency due to inertial impaction.

Brownian diffusion The collection efficiency due to particle diffusion to the front surface of a filter can be calculated using an expression proposed by Manton [21],

$$E_{\mathrm{D}} = 1 - \exp\left(\frac{-\alpha_1 \mathrm{Pe}^{-2/3}}{1 + (\alpha_1/\alpha_2)\mathrm{Pe}^{-7/15}}\right) \tag{11}$$

$$\alpha_1 = 4.57 - 6.46 P_{\mathrm{grid}} + 4.58 P_{\mathrm{grid}}^2 \tag{12}$$

$$\alpha_2 = 4.5, \tag{13}$$

where Pe is the Peclet's number given by $\mathrm{Pe} = D_0 U_0 / D$, D_0 is the grid hole diameter, U_0 is the frontal velocity, P_{grid} is the grid porosity, α_1 and α_2 were determied from a least-squares fitting for $0.05 < P_{\mathrm{grid}} < 0.64$. D is the particle diffusion coefficient,

$$D = \frac{k_{\mathrm{B}} T C_c}{6\pi\mu R}, \tag{14}$$

where k_B is the Boltzmann constant, T is the temperature, μ is the gas dynamic viscosity, R is the particle radius. C_c is the Cunningham slip correction factor given by

$$C_c = 1 + \mathrm{Kn}(1.257 + 0.4\exp(-1.1/\mathrm{Kn})), \tag{15}$$

where Kn is the Knudsen number defined as λ/R and λ is the mean free path of the gas molecules.

Inertial impaction The collection efficiency due to particle impaction is calculated using a formulation proposed by Pich [30] as follows,

$$E_I = \frac{2\varepsilon_I}{1+\xi} - \left(\frac{\varepsilon_I}{1+\xi}\right)^2 \tag{16}$$

$$\varepsilon_I = 2\mathrm{Stk}\sqrt{\xi} + 2\mathrm{Stk}^2\xi \exp\left(-\frac{1}{Stk\sqrt{\xi}}\right) - 2\mathrm{Stk}^2\xi \tag{17}$$

$$\xi = \frac{\sqrt{P_{\mathrm{grid}}}}{1-\sqrt{P_{\mathrm{grid}}}}, \tag{18}$$

where Stk is the Stokes number given by

$$\mathrm{Stk} = \frac{4\rho_s R^2 U_0 C_c}{9\mu D_0}, \tag{19}$$

and ρ_s is the particle density.

In this analysis, the particle size is assumed to be equal to the spherical equivalent size from projected area analysis, i.e. $2R = d_{\mathrm{sph}}$. This assumption is a valid approximation given that the particles observed on the TEM are mostly single primaries with some small aggregates (discussed further in Section 4.2). The parameters used in the calculation of TEM grid collection efficiency (Eq. 10) are given in Table 1. The face velocity is approximately 14 m/s, estimated from the total flow rate flowing through the filter (27 lpm) and the tube cross-section area (32 mm^2). However, the actual face velocity is likely to be lower due to flow divergence on the TEM surface. As an estimate, two different face velocities are tested here, 14 and 7 m/s. The hole diameter and grid porosity are taken from Ref. [32] for a typical holey carbon grid. The density of anatase is used for particles prepared in $\phi = 0.35$ flames while density of rutile is used for $\phi = 1.67$ [23, 25].

Table 1: *Parameters used for size-dependent collection efficiency calculation.*

Parameters	Short description	Value	Notes
λ	Mean free path	70.9 nm	N_2 at 313.15 K, 1 atm
μ	Gas dynamic viscosity	1.85×10^{-5} kg/m/s	N_2 at 313.15 K
ρ_s	Anatase density	3780 kg/m^3	For $\phi = 0.35$
	Rutile density	4250 kg/m^3	For $\phi = 1.67$
T	Gas temperature	313.15 K	Experimental condition
U_0	Face velocity	7 and 14 m/s	Experimental condition
D_0	Hole diameter	1.67 μm	[32]
P_{grid}	Grid porosity	0.4	[32]

The calculated collection efficiency is shown in Fig. 4(a). This correction is applied to the aggregate size distributions from the TEM image analysis. In order to demonstrate the effect of this correction across the conditions studied in this work, the median spherical-equivalent particle sizes, $\langle d_{\mathrm{sph}} \rangle$, for $\phi = 0.35$ flame, before and after correction, are plotted

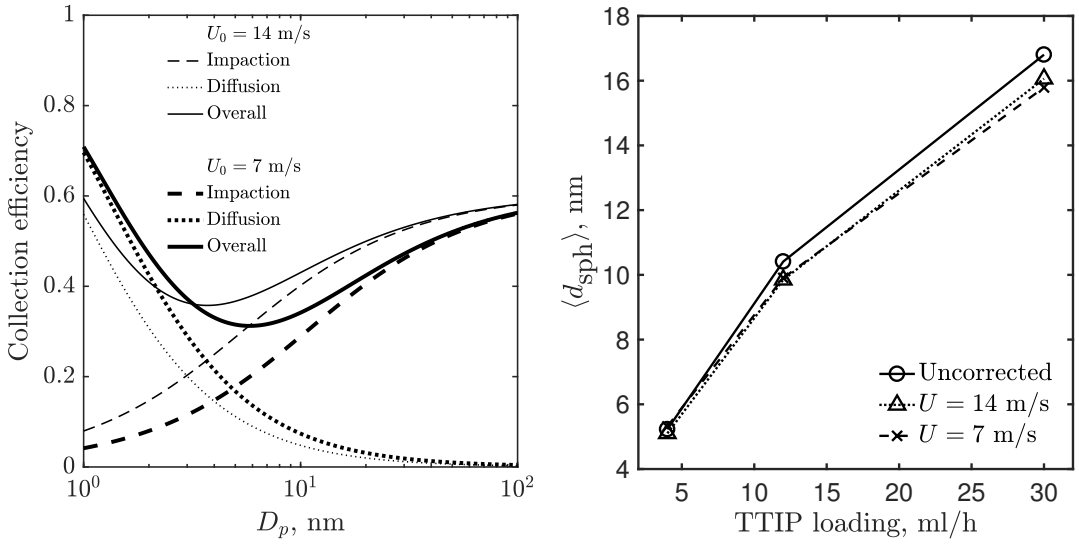

Figure 4: *(a) The collection efficiencies calculated based on Eqs. 10, 11, and 16 with face velocities, U, of 7 and 14 m/s (thick and thin lines, respectively), using anatase density. (b) The median spherical-equivalent particle sizes, $\langle d_{sph} \rangle$, before and after collection efficiency correction for $\phi = 0.35$ flames. The lines are added as a visual aid.*

in Fig. 4(b). It is noted that the correction is relatively small, especially for small TTIP loadings which is due to narrow particle distributions. In addition, the correction seems to be almost insensitive to the choice of face velocity. Subsequently, similar correction with $U = 7$ m/s is applied to all TEM aggregate particle size distributions presented in this work. This correction, however, is not applied for primary particle size distributions as the collection efficiency is a function of the aggregate size.

4.1.2 Comparison with electrical mobility measurements

The DMS500 used in this study was calibrated at the factory against a differential mobility analyzer (DMA). Here, calibration for spherical particles with a monomodal distribution was used. The Stokes-Cunningham formula for electrical mobility, Z, used with the DMA, is given by

$$Z/q = \frac{C_c}{6\pi\mu R}, \tag{20}$$

where q is the charge in the particle. The empirical Stokes-Cunningham formula is typically consistent with Eipstein's formula assuming a diffuse scattering model. However, it has been shown that in the limit of Kn $>>$ 1, the mobility particle size based on the Stokes-Cunningham formula tends to be over-predicted by 10–20% compared to particle size from electron microscopy due to increasing influence of long-range potential forces on particle scattering [15, 18, 33].

Li and Wang [17] suggests a generalised expression that accounts for gas-particle interactions in Kn $>>$ 1 limit,

$$Z/q = \frac{3}{8}\frac{1}{\sqrt{2\pi m_r k_B T} N_g R^2 \Omega_{avg}^{(1,1)^*}} \tag{21}$$

$$\Omega_{avg}^{(1,1)^*} = \varphi\Omega_d^{(1,1)^*} + (1-\varphi)\Omega_s^{(1,1)^*}, \tag{22}$$

where m_r is the reduced mass of the gas molecule, m_g, and particle, m_p, such that $m_r = m_g m_p/(m_g+m_p)$, N_g is the gas number density given by ρ_g/m_g, ρ_g is the gas density. φ is the empirical momentum-accommodation function given by

$$\varphi = \frac{1+0.9\mathrm{Kn}\{1-1/[1+(R/2.5)^{15}]\}}{1+\mathrm{Kn}}. \tag{23}$$

$\Omega_d^{(1,1)^*}$ and $\Omega_s^{(1,1)^*}$ are reduced collision integrals, parameterised as functions of σ', a non-dimensionalised collision diameter, and T^*, a modified reduced temperature,

$$\Omega_d^{(1,1)^*} = 1 + \frac{\pi}{8} + \left[1.072 + \frac{2.078}{T^{*1/4}} + \frac{1.261}{T^{*1/2}}\right]\sigma' + \left[3.285 - \frac{8.872}{T^{*1/4}} + \frac{5.225}{T^{*1/2}}\right]\sigma'^2 \tag{24}$$

$$\Omega_s^{(1,1)^*} = 1 + \left[0.316 + \frac{1.47}{T^{*1/4}} + \frac{0.476}{T^{*1/2}}\right]\sigma' + \left[1.53 - \frac{5.013}{T^{*1/4}} + \frac{4.025}{T^{*1/2}}\right]\sigma'^2. \tag{25}$$

The parameters σ' and T^* are related to the Lennard-Jones 12-6 parameters, i.e. wall depth, ε, and collision diameter, σ, for the interaction between a fluid molecule and a constituent atom or molecule of the particle, as follows,

$$\sigma' = \frac{\sigma}{R} \tag{26}$$

$$T^* = \frac{3Vk_BT}{2\pi\varepsilon\sigma^3}, \tag{27}$$

where V is the effective volume of the particle per molecule given by $\bar{M}/\rho_s$, $\bar{M}$ is the mean atomic mass of particle material, and ρ_s is the mass density of the particle. The interaction potential parameters, σ and ε, can be estimated from the combination rules $\sigma = (\sigma_g+\sigma_s)/2$ and $\varepsilon = \sqrt{\varepsilon_g\varepsilon_s}$, where subscripts g and s denote the gas molecule and particle molecule or atom.

The parameters σ_s and ε_s for TiO_2 are estimated using the melting point, T_m, and the mass density at melting point, ρ_{s,T_m}, of TiO_2, such that $\varepsilon_s = 1.92kT_m$, and $\sigma_s = \sqrt[3]{1.8\bar{M}/\rho_{s,T_m}}$ [33]. Here the melting point of TiO_2 is taken as 2250 K and the density at melting point is 3210 kg/m^3 [1]. The parameters used in this section are summarised in Table 2. Similar to the TEM collection efficiency correction, the density of anatase is used for particles prepared in $\phi = 0.35$ flames while density of rutile is used for $\phi = 1.67$ [23, 25].

The correction to the mobility diameter is performed by firstly calculating the electrical mobility, Z/q, based on Eqs. 15 and 20 using the median mobility radius (from log-normal fitting of mobility size distributions) reported from the DMS (i.e. $2R = 2R_{DMS} = \langle d_m \rangle$). The working pressure and temperature of the DMS used in this analysis are 250 mbar and

Table 2: *Parameters used for mobility size correction.*

Parameters	Short description	Value	Notes
μ	Gas viscosity	1.89×10^{-5} kg/m/s	N_2 at 323.15 K
λ	Mean free path	294 nm	N_2 at 323.15 K, 250 mbar
ε_g	L-J 12-6 parameter	98.4 K	N_2 [18]
σ_g	L-J 12-6 parameter	3.652 Å	N_2 [18]
ε_s	L-J 12-6 parameter	4320 K	TiO_2
σ_s	L-J 12-6 parameter	4.193 Å	TiO_2
m_g	Gas molecule mass	28.0 g/mol	N_2
ρ_g	Gas density	0.261 kg/m^3	N_2 at 323.15 K, 250 mbar
$\bar{M}$	Particle mass	79.9 g/mol	TiO_2
ρ_s	Anatase density	3780 kg/m^3	For $\phi = 0.35$
	Rutile density	4250 kg/m^3	For $\phi = 1.67$
T	Temperature	323.15 K	Experimental condition

50°C. The calculated Z/q is then used to calculate the corrected particle size according to Eq. 21 where $\Omega_{\text{avg}}^{(1,1)^*}$ is calculated using $R = R_{\text{TEM}}$.

Figure 5(a) shows the uncorrected mobility size distribution as well as the spherical-equivalent size distribution obtained from the TEM image analysis for $\phi = 1.67$ and 4 ml/h TTIP loading where the mobility measurement overpredicts the particle size by approximately 25%. This is consistent with previous studies comparing mobility and microscopy sizes where average overprediction of 20% was reported [15, 33].

The uncorrected and corrected mobility sizes are compared with the spherical-equivalent sizes for all cases in this work, shown in Fig 5(b). The comparison is further summarised in Table 3. Here, the spherical-equivalent size from TEM image analysis is taken as the "actual" particle size, i.e. $2R_{\text{TEM}} = \langle d_{\text{sph}} \rangle$, given a significant proportion of the particles are spherical as discussed further in the next section. As expected, the discrepancy for uncorrected mobility size is greatest for the smallest particles. The correction applied reduces the average difference from 21% to 5%, similar to the average difference reported by Li and Wang [18] for previous experimental data.

The good agreement between the corrected mobility particle size and TEM-derived particle size confirms that the sampling methodology used in this work can be used to characterise the morphology of small nano-aggregates as discussed in the next section.

4.2 Particle morphology

Figure 6 shows the measured primary particle sizes from the TEM images with high magnification (150,000×). It is noted that the variation for higher loading cases are likely to be exaggerated due to the smaller number of primaries per image (as primary particles are larger). It is important to point out that due to the resolution limit, poorer contrast, and higher chance of overlap, smaller particles are harder to measure manually (with only

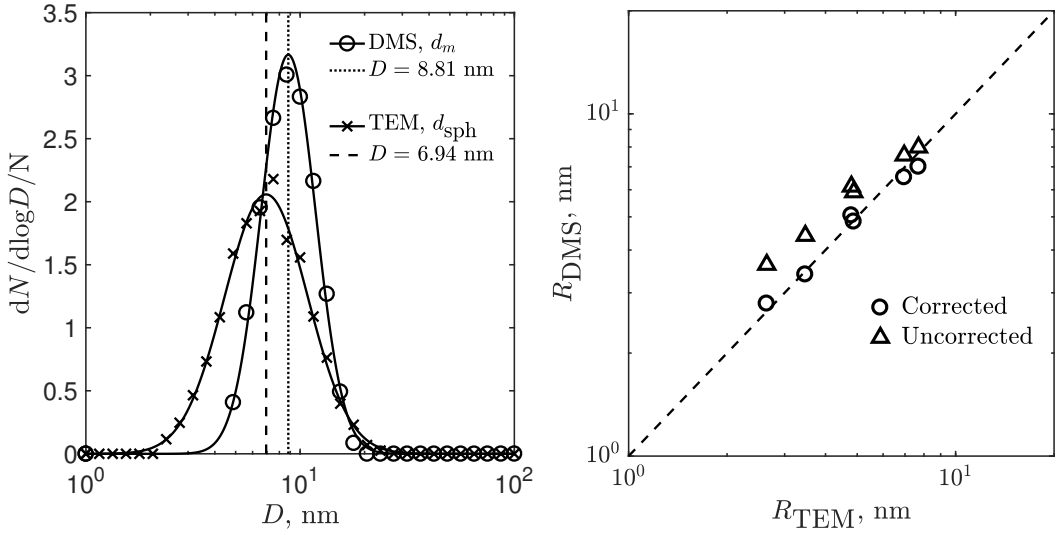

(a) (b)

Figure 5: *(a) Particle size distributions measured using DMS, d_m, and from TEM image analysis (d_{sph}) for $\phi = 1.67$ and 4 ml/h TTIP condition. The vertical lines indicate the median values from log-normal fit to the distributions used in the correction. (b) Comparison between TEM-derived sizes, R_{TEM}, and the mobility sizes, R_{DMS}, corrected and uncorrected.*

Table 3: *Particle sizes from TEM projected area analysis and mobility measurements, before and after correction, with the DMS.*

ϕ	TTIP (ml/h)	TEM	DMS		DMS, corrected	
		$\langle d_{\mathrm{sph}} \rangle$, nm	$\langle d_m \rangle$, nm	Error, %	$\langle d_m \rangle$, nm	Error, %
0.35	4	5.29	7.25	37.1	5.76	5.5
0.35	12	9.60	12.27	27.8	10.10	5.2
0.35	30	15.40	15.96	3.6	14.00	-9.0
1.67	4	6.94	8.81	26.9	6.79	-2.2
1.67	12	9.76	11.81	21.0	9.69	-0.8
1.67	30	13.92	15.12	8.6	13.05	-6.2
		Mean absolute error, %		20.8		4.8

particles larger than approximately 3 nm can be confidently identified). This is likely to result in slight bias towards larger particles. As such, the Sauter mean diameter, $\bar{d}_{3/2}$, is reported here in addition to the averaged mean, $\bar{d}_p$, as it tends to represent data closer to the right end of the distribution.

It is immediately obvious from Fig. 6 that the primary sizes are strongly affected by the TTIP loading but are relatively insensitive to the flame temperature. This is surprising as the rich flame ($\phi = 1.67$) is approximately 450 K hotter than the lean flame ($\phi = 0.35$). This result is consistent with our previous measurements where we showed that the primary particle sizes from flames with a wide range of equivalence ratios with the same

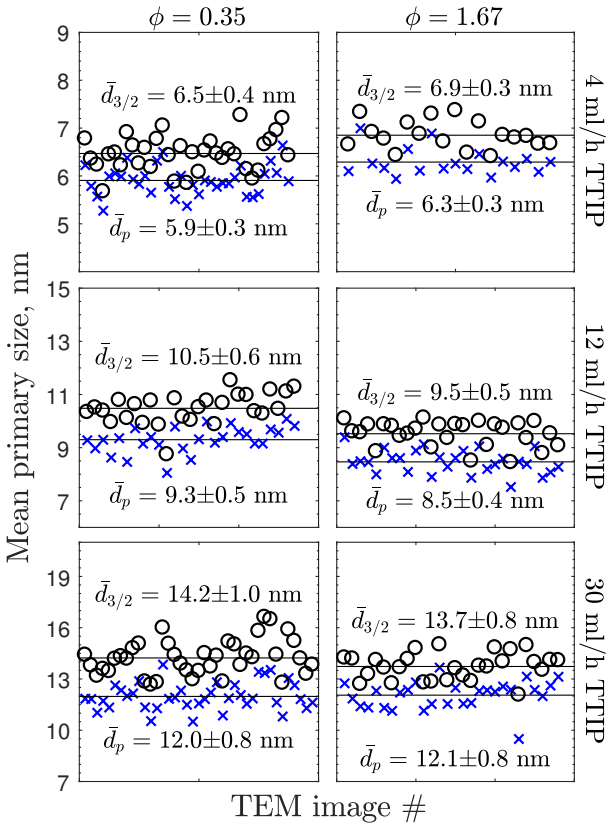

Figure 6: *Mean primary sizes, number-averaged $\bar{d}_p$ and Sauter-mean $\bar{d}_{3/2}$, for individual TEM images analysed. The uncertainties given are assumed to be equal to the standard deviation of average sizes for individual images. The overall mean primary sizes for each condition tested are shown with the horizontal solid lines.*

TTIP loading are similar [23]. The insensitivity of particle size to the maximum flame temperature was explained by the reduced particle residence time in hotter flames due to a higher convective velocity.

Figure 7 shows the TEM images used for the aggregate projected area analysis (see Section 3). The particle morphology can be described as a mixture of single spherical particles and small aggregates with small degree of sintering. High magnification experimental TEM images, not shown here, reveal highly crystalline primary particles. These observations are in agreement with previous studies [25, 36].

In order to describe the particle morphology, α, the ratio of d_g to d_{sph}, is used to characterise the level of particle aggregation. Spherical particles have α close to 0.7 while aggregates with open structure have a larger α. As α is affected by the pixel resolution of the particles, the image magnifications were adjusted for different TTIP loading cases such that the average number of pixels per particle is conserved. This ensures that the particle morphology as characterised by α is comparable across all loadings tested.

Figure 8 shows examples of typical aggregates observed in the aggregate size analysis with their corresponding α. Spherical particles (Fig. 8(a)) are typically characterised by

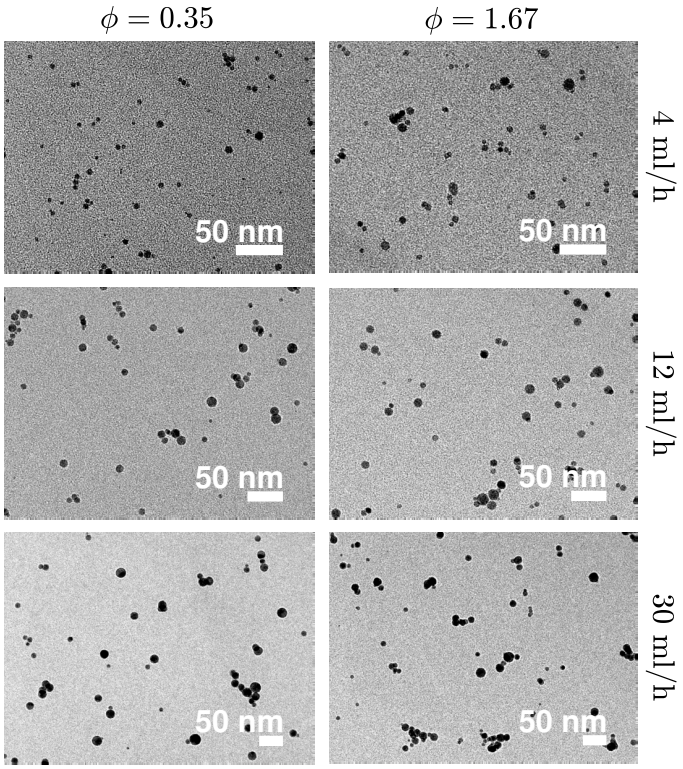

Figure 7: *Examples of TEM images used for aggregate size analysis for all conditions tested in this work. In order to minimise bias from particles overlapping, only TEM images with a particle coverage of less than 5% were included in the analysis.*

α around 0.7. As the structure becomes more open and non-spherical, α, increases to a maximum of around 1.3.

Figure 9 shows the bivariate histograms of all particles analysed in this work characterised by the parameters d_{sph} and α. Two important observations are made here: First, a significant proportion of particles have α close to 0.7 (shown by the color scale). This is consistent with the qualitative observation that most particles have spherical morphology. Second, larger particles tend to have larger α which is expected as larger particles sinter more slowly leading to the formation of more open structures.

In this work, a condition of $\alpha < 0.73$ is assumed to define a spherical particle. This is slightly higher than a perfect circle whose $\alpha = 0.71$ to allow for some degree of roughness from image analysis algorithm. Table 4 summarises the important metrics of the particle morphology obtained from the aggregate image analysis. Taking into account the size-dependent collection efficiency, $E(d)$ (discussed in Section 4.1.1), an average property, $\bar{X}$, can be calculated as follows

$$\bar{X} = \frac{\sum_i^N X_i / E(d_{\text{sph},i})}{\sum_i^N 1 / E(d_{\text{sph},i})}. \tag{28}$$

In all cases, the value of $\bar{\alpha}$, lies within a narrow range of 0.75–0.77 indicating a small degree of particle aggregation which is almost insensitive to the conditions tested. The

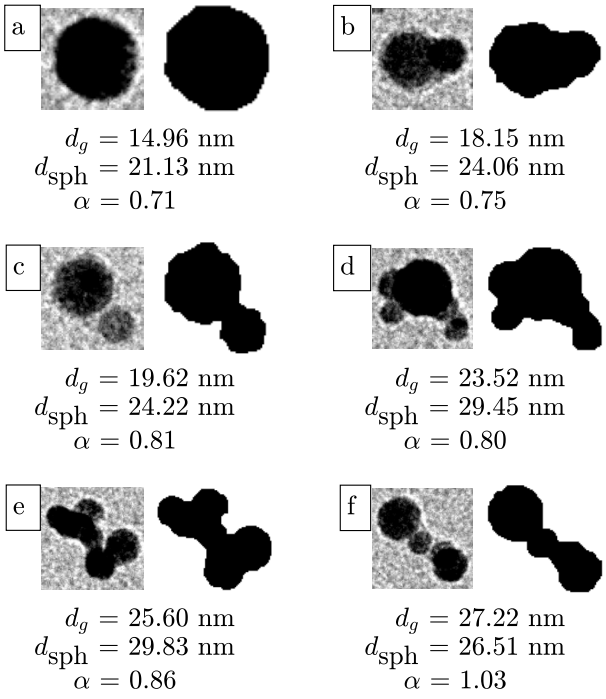

Figure 8: *Examples of particles observed in the TEM image analysis and the corresponding pixel mask at varying degree of aggregation (with $\alpha = d_g/d_{sph}$ ranging from 0.7 to 1). A spherical particle is defined as having $\alpha < 0.73$ in this work.*

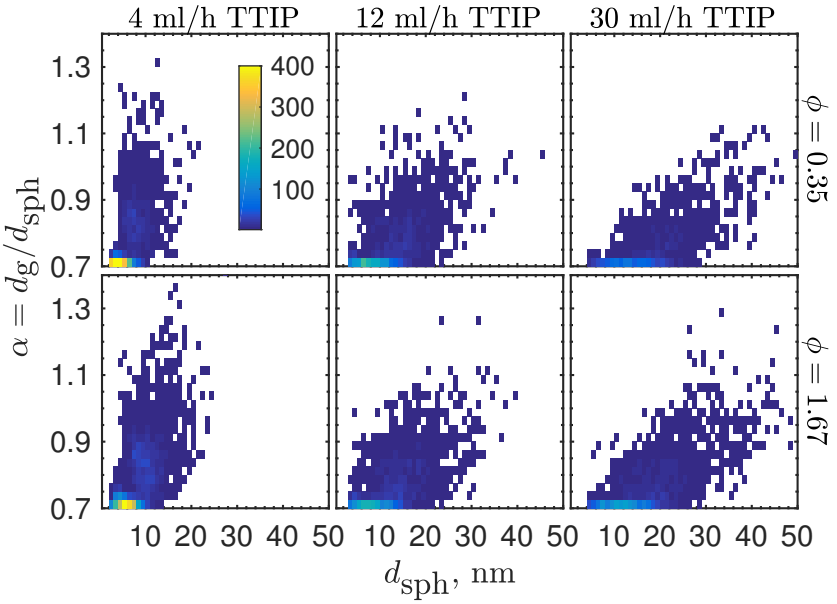

Figure 9: *Bivariate histograms of all particles analysed in this work characterised by their geometric parameters d_{sph} and α. The color scale represents particle count. The bin sizes are 1 nm and 0.025 for d_{sph} and α, respectively.*

degree of aggregation can be further quantified by the proportion of particles with spherical morphology ($\alpha < 0.73$), f, which ranges from 57–68%. This significant proportion

of single spherical particles justifies the choice of using d_{sph} as the particle size for TEM collection efficiency and mobility size corrections discussed in Section 4.1.

Table 4: *Summary of aggregate size analysis (after size-dependent collection efficiency correction).*

ϕ	TTIP (ml/h)	All aggregates				Aggregates with $\alpha < 0.73$		
		count	$\bar{d}_{\mathrm{sph}}$, nm	$\bar{d}_g$, nm	$\bar{\alpha}$	f,[a] %	$\bar{d}^*_{\mathrm{sph}}$, nm	Δ,[b] %
0.35	4	3016	5.81	4.54	0.76	68	4.71	-20.2
0.35	12	2601	10.78	8.37	0.75	64	8.37	-10.0
0.35	30	1582	17.00	13.20	0.75	62	13.27	10.75
1.67	4	3823	7.62	6.10	0.77	57	5.96	-5.2
1.67	12	2676	10.96	8.53	0.76	61	8.45	-0.2
1.67	30	2633	15.49	12.07	0.75	62	11.89	-1.3

[a] $f = [\sum_{\alpha_i<0.73} 1/E(d_{\mathrm{sph},i})]/[\sum_{\mathrm{all}\ i} 1/E(d_{\mathrm{sph},i})]$
[b] $\Delta = (\bar{d}^*_{\mathrm{sph}} - \bar{d}_p)/\bar{d}_p$ (values of $\bar{d}_p$ from Fig. 6)

Further, the primary size distributions are compared to the aggregate size distributions from the projected area analysis in Fig. 10. In general, the aggregate size distributions, d_{sph}, are broader than the primary size distributions, d_p, but the modes of distributions are similar due to the high proportion of single primary particles. The size distributions of particles with $\alpha < 0.73$, denoted as d^*_{sph}, are also shown. It is interesting to note that d^*_{sph} and d_p distributions show relatively good agreement. This suggests that the use of $\alpha < 0.73$ to isolate the spherical particles is appropriate.

A rather significant discrepancy is observed for the 4 ml/h case for $\phi = 0.35$ (20%, Table 4). The disagreement between $\bar{d}^*_{\mathrm{sph}}$ from aggregate size analysis and $\bar{d}_p$ from primary particle analysis is likely a result of a bias in the latter towards large particles. This is due to poor contrast and particle overlap especially when the particles are smaller than 4 nm. The comparison of the Sauter mean diameters, $\bar{d}_{3/2}$, for this case shows a smaller difference of 10% suggesting that the discrepancy mainly comes from the left tail of the distribution (small particles).

Lastly, the relatively good agreement between d^*_{sph} and d_p over all conditions tested suggests that the aggregation does not occur in flame but near the stagnation plate. This is plausible as the gas temperature only decreases steeply near the stagnation plate [22, 36]. This is supported by the observation that the primary particles in the aggregates are mostly in point contact with small degree of sintering (see Fig. 7).

5 Conclusions

In this work, we demonstrated the use of a TEM sampling method that relies on impaction and diffusion in order to characterise the morphology of titania nano-aggregates in a stagnation flame reactor. TEM images were taken and semi-automated image analysis procedures were performed. The method is validated against electrical mobility measurements

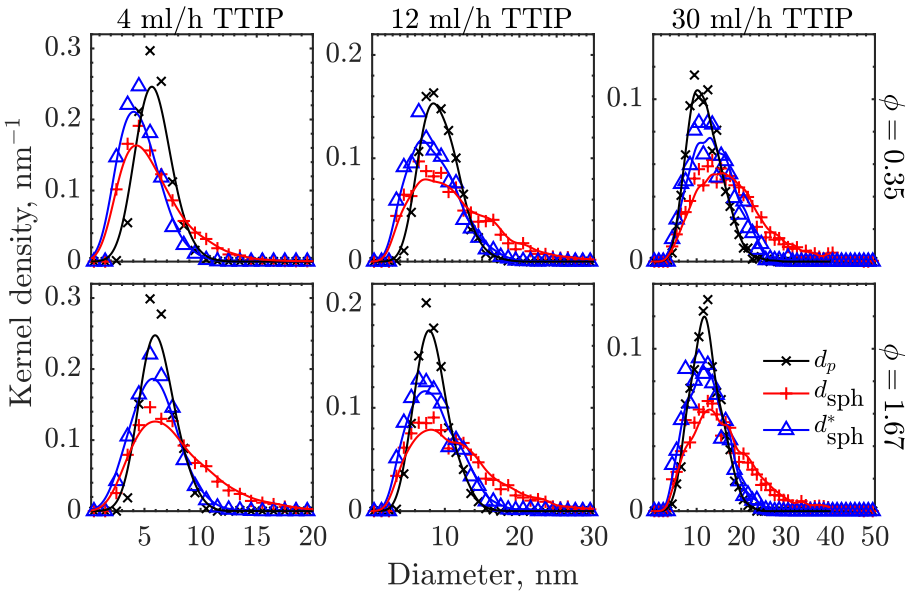

Figure 10: *The primary diameter, d_p, and spherical equivalent diameter from aggregate projected area, d_{sph}, distributions for all conditions tested. d^*_{sph} is the spherical equivalent diameter of aggregates with $\alpha < 0.73$ (single primaries). The bin size and the bandwidth for kernel density estimation are 1 nm.*

taking into account size-dependent collection efficiency of the TEM sampling and mobility size correction. The excellent agreement between TEM-derived and mobility sizes suggests that the TEM sampling combined with image analysis can be used to characterise the particle morphology for the conditions presented here.

The analysis reveals that the primary particle and aggregate sizes are mostly affected by the precursor loading but not the flame temperature. In contrast, the degree of aggregation is found to be insensitive to the precursor loading or the flame temperature. The degree of aggregation is described by α, the ratio of gyration to spherical-equivalent diameters, where spherical particles are defined as having $\alpha < 0.73$. Approximately 60–70% particles analysed have spherical morphology (single spherical particles) while the rest form small aggregated structure with $\alpha = 0.73$–1.3. The primary particle size distributions are similar to the spherical particle size distributions which suggests that the aggregation only occurs very late in the particle growth stage (i.e. near the stagnation plate). This is consistent with the qualitative observation of minimal sintering level in the aggregates.

6 Acknowledgements

This project is supported by the National Research Foundation (NRF), Prime Minister's Office, Singapore under its Campus for Research Excellence and Technological Enterprise (CREATE) programme. The authors thank CMCL Innovations for generous financial support. MK also acknowledges the support of the Alexander von Humboldt Foundation.

References

[1] O. L. G. Alderman, L. B. Skinner, C. J. Benmore, A. Tamalonis, and J. K. R. Weber. Structure of molten titanium dioxide. *Phys. Rev. B - Condens. Matter Mater. Phys.*, 90(9):1–13, 2014. doi:10.1103/PhysRevB.90.094204.

[2] H. M. Amin, A. Bennett, and W. L. Roberts. Determining fractal properties of soot aggregates and primary particle size distribution in counterflow flames up to 10 atm. *Proc. Combust. Inst.*, 37, 2018. doi:10.1016/j.proci.2018.07.057.

[3] O. I. Arabi-Katbi, S. E. Pratsinis, P. W. Morrison, and C. M. Megaridis. Monitoring the flame synthesis of TiO_2 particles by in-situ FTIR spectroscopy and thermophoretic sampling. *Combust. Flame*, 124(4):560–572, 2001. doi:10.1016/S0010-2180(00)00227-3.

[4] M. Balthasar and M. Kraft. A stochastic approach to calculate the particle size distribution function of soot particles in laminar premixed flames. *Combust. Flame*, 133(3):289–298, 2003. doi:10.1016/S0010-2180(03)00003-8.

[5] A. Bescond, J. Yon, F. X. Ouf, D. Ferry, D. Delhaye, D. Gaffié, A. Coppalle, and C. Rozé. Automated determination of aggregate primary particle size distribution by TEM image analysis: Application to soot. *Aerosol Sci. Technol.*, 48(8):831–841, 2014. doi:10.1080/02786826.2014.932896.

[6] M. L. Botero, N. Eaves, J. A. Dreyer, Y. Sheng, J. Akroyd, W. Yang, and M. Kraft. Experimental and numerical study of the evolution of soot primary particles in a diffusion flame. *Proc. Combust. Inst.*, 37, 2018. doi:10.1016/j.proci.2018.06.185.

[7] J. Camacho, A. V. Singh, W. Wang, R. Shan, E. K. Y. Yapp, D. Chen, M. Kraft, and H. Wang. Soot particle size distributions in premixed stretch-stabilized flat ethylene-oxygen-argon flames. *Proc. Combust. Inst.*, 36(1):1001–1009, 2017. doi:10.1016/j.proci.2016.06.170.

[8] M. F. Chandler, T. Yingwu, and Ü. Ö. Köylü. Diesel engine particulate emissions: A comparison of mobility and microscopy size measurements. *Proc. Combust. Inst.*, 31 II:2971–2979, 2007. doi:10.1016/j.proci.2006.07.200.

[9] M. Frenklach and S. J. Harris. Aerosol dynamics modeling using the method of moments. *J. Colloid Interface Sci.*, 118(1):252–261, 1987. doi:10.1016/0021-9797(87)90454-1.

[10] R. C. Gonzalez, R. E. Woods, S. L. Eddins, et al. *Digital image processing using MATLAB.*, volume 624. Pearson-Prentice-Hall, 2004.

[11] D. Hou, C. S. Lindberg, M. Y. Manuputty, Y. Xiaoqing, and M. Kraft. Modelling soot formation in a benchmark ethylene stagnation flame with a new detailed population balance model. *Submitted for publication*, 2018.

[12] N. J. Kempema and M. B. Long. Combined optical and TEM investigations for a detailed characterization of soot aggregate properties in a laminar coflow diffusion flame. *Combust. Flame*, 164:373–385, 2016. doi:10.1016/j.combustflame.2015.12.001.

[13] O. P. Korobeinichev, A. G. Shmakov, R. A. Maksyutov, A. G. Tereshchenko, D. A. Knyazkov, T. A. Bolshova, M. L. Kosinova, V. S. Sulyaeva, and J. S. Wu. Synthesis of mesoporous nanocrystalline TiO_2 films in a premixed H_2/O_2/Ar flame. *Combust. Explos. Shock Waves*, 48(1):49–56, 2012. doi:10.1134/S0010508212010078.

[14] M. Kraft. Modelling of particulate processes. *KONA Powder Part. J.*, 23(March): 18–35, 2005. doi:10.14356/kona.2005007.

[15] Y. Kuga, K. Okauchi, D. Takeda, Y. Ohira, and K. Ando. Classification performance of a low pressure differential mobility analyzer for nanometer-sized particles. *J. Nanoparticle Res.*, 3(2-3):175–183, 2001. doi:10.1023/A:1017952821121.

[16] S. Li, Y. Ren, P. Biswas, and S. D. Tse. Flame aerosol synthesis of nanostructured materials and functional devices: Processing, modeling, and diagnostics. *Prog. Energy Combust. Sci.*, 55:1–59, 2016. doi:10.1016/j.pecs.2016.04.002.

[17] Z. Li and H. Wang. Drag force, diffusion coefficient, and electric mobility of small particles. I. Theory applicable to the free-molecule regime. *Phys. Rev. E*, 68(6):1–9, 2003. doi:10.1103/PhysRevE.68.061206.

[18] Z. Li and H. Wang. Drag force, diffusion coefficient, and electric mobility of small particles. II. Application. *Phys. Rev. E*, 68(6):061207, 2003. doi:10.1103/PhysRevE.68.061207.

[19] C. S. Lindberg, M. Y. Manuputty, J. Akroyd, and M. Kraft. A two-step simulation methodology for modelling stagnation flame synthesised aggregated nanoparticles. *Submitted for publication*, 2018.

[20] C. S. Lindberg, M. Y. Manuputty, E. Yapp, J. Akroyd, and M. Kraft. A new detailed particle model for polydisperse titanium dioxide aggregates. *Submitted for publication*, 2018.

[21] M. J. Manton. Brownian diffusion of aerosols to the face of a nuclepore filter. *Atmos. Environ.*, 13(4):525–531, 1979. doi:10.1016/0004-6981(79)90146-X.

[22] M. Y. Manuputty, J. Akroyd, S. Mosbach, and M. Kraft. Modelling TiO_2 formation in a stagnation flame using method of moments with interpolative closure. *Combust. Flame*, 178:135–147, 2017. doi:10.1016/j.combustflame.2017.01.005.

[23] M. Y. Manuputty, J. A. H. Dreyer, Y. Sheng, E. J. Bringley, M. L. Botero, J. Akroyd, and M. Kraft. Polymorphism of nanocrystalline TiO_2 prepared in a stagnation flame: Formation of TiO_2-II phase. *Submitted for publication*, 2018.

[24] MATLAB Image Processing Toolbox. Matlab image processing toolbox, 2016b. The MathWorks.

[25] S. Memarzadeh, E. D. Tolmachoff, D. J. Phares, and H. Wang. Properties of nanocrystalline TiO_2 synthesized in premixed flames stabilized on a rotating surface. *Proc. Combust. Inst.*, 33(2):1917–1924, 2011. doi:10.1016/j.proci.2010.05.065.

[26] W. J. Menz and M. Kraft. The suitability of particle models in capturing aggregate structure and polydispersity. *Aerosol Sci. Technol.*, 47(7):734–745, 2013. doi:10.1080/02786826.2013.788244.

[27] W. J. Menz and M. Kraft. A new model for silicon nanoparticle synthesis. *Combust. Flame*, 160(5):947–958, 2013. doi:10.1016/j.combustflame.2013.01.014.

[28] I. Ogura, N. Hashimoto, M. Kotake, H. Sakurai, A. Kishimoto, and K. Honda. Aerosol particle collection efficiency of holey carbon film-coated TEM grids. *Aerosol Sci. Technol.*, 48(7):758–767, 2014. doi:10.1080/02786826.2014.924614.

[29] F. X. Ouf, J. Yon, P. Ausset, A. Coppalle, and M. Maillé. Influence of sampling and storage protocol on fractal morphology of soot studied by transmission electron microscopy. *Aerosol Sci. Technol.*, 44(11):1005–1017, 2010. doi:10.1080/02786826.2010.507228.

[30] J. Pich. Impaction of aerosol particles in the neighbourhood of a circular hole. *Collect. Czech. Chem. Commun*, 29(9):2223–2227, 1964. doi:10.1135/cccc19642223.

[31] Y. Ren, J. Wei, and S. Li. In-situ laser diagnostic of nanoparticle formation and transport behavior in flame aerosol deposition. *Proc. Combust. Inst.*, 37, 2018. doi:10.1016/j.proci.2018.06.015.

[32] B. R'Mili, O. L. Le Bihan, C. Dutouquet, O. Aguerre-Charriol, and E. Frejafon. Particle sampling by TEM grid filtration. *Aerosol Sci. Technol.*, 47(7):767–775, 2013. doi:10.1080/02786826.2013.789478.

[33] V. Y. Rudyak, S. L. Krasnolutskii, a. G. Nasibulin, and E. I. Kauppinen. Methods of measuring the diffusion coefficient and sizes of nanoparticles in a rarefied gas. *Dokl. Phys.*, 47(10):758–761, 2002. doi:10.1134/1.1519325.

[34] S. Shekar, W. J. Menz, A. J. Smith, M. Kraft, and W. Wagner. On a multivariate population balance model to describe the structure and composition of silica nanoparticles. *Comput. Chem. Eng.*, 43:130–147, 2012. doi:10.1016/j.compchemeng.2012.04.010.

[35] Y. Sheng, M. Kraft, and R. Xu. Emerging applications of nanocatalysts synthesized by flame aerosol processes. *Curr. Opin. Chem. Eng.*, 20:39–49, 2018. doi:10.1016/j.coche.2018.01.009.

[36] E. D. Tolmachoff, A. D. Abid, D. J. Phares, C. S. Campbell, and H. Wang. Synthesis of nano-phase TiO_2 crystalline films over premixed stagnation flames. *Proc. Combust. Inst.*, 32 II(2):1839–1845, 2009. doi:10.1016/j.proci.2008.06.052.

[37] S. Tsantilis and S. E. Pratsinis. Narrowing the size distribution of aerosol-made titania by surface growth and coagulation. *J. Aerosol Sci.*, 35(3):405–420, 2004. doi:10.1016/j.jaerosci.2003.09.006.

[38] S. Tsantilis, H. K. Kammler, and S. E. Pratsinis. Population balance modeling of flame synthesis of titania nanoparticles. *Chem. Eng. Sci.*, 57(12):2139–2156, 2002. doi:10.1016/S0009-2509(02)00107-0.

[39] C. Wang, Q. N. Chan, R. Zhang, S. Kook, E. R. Hawkes, G. H. Yeoh, and P. R. Medwell. Automated determination of size and morphology information from soot transmission electron microscope (TEM)-generated images. *J. Nanoparticle Res.*, 18(5):1–15, 2016. doi:10.1007/s11051-016-3434-x.

[40] J. Warnatz, U. Maas, and R. W. Dibble. *Combustion: Physical and chemical fundamentals, modelling and simulation, experiments, pollutant formation*. Springer, 4th edition, 2006.

[41] Y. Xiong and S. E. Pratsinis. Formation of agglomerate particles by coagulation and sintering — Part {I}. {A} Two dimensional solution of the population balance equation. *J. Aerosol Sci.*, 24(3):283–300, 1993. doi:10.1016/0021-8502(93)90003-R.

[42] E. K. Y. Yapp, D. Chen, J. Akroyd, S. Mosbach, M. Kraft, J. Camacho, and H. Wang. Numerical simulation and parametric sensitivity study of particle size distributions in a burner-stabilised stagnation flame. *Combust. Flame*, 162(6):2569–2581, 2015. doi:10.1016/j.combustflame.2015.03.006.

[43] B. Zhao, K. Uchikawa, J. R. McCormick, C. Y. Ni, J. G. Chen, and H. Wang. Ultrafine anatase TiO_2 nanoparticles produced in premixed ethylene stagnation flame at 1 atm. *Proc. Combust. Inst.*, 30(2):2569–2576, 2005. doi:10.1016/j.proci.2004.08.146.

[44] B. Zhao, K. Uchikawa, and H. Wang. A comparative study of nanoparticles in premixed flames by scanning mobility particle sizer, small angle neutron scattering, and transmission electron microscopy. *Proc. Combust. Inst.*, 31 I:851–860, 2007. doi:10.1016/j.proci.2006.08.064.